RESEARCH ARTICLE

WILEY

A three-dimensional hybrid finite element — spectral boundary integral method for modeling earthquakes in complex unbounded domains

Gabriele Albertini[1,2] | **Ahmed E. Elbanna**[3] | **David S. Kammer**[1]

[1]Institute for Building Materials, ETH Zurich, Zurich, Switzerland

[2]School of Civil and Environmental Engineering, Cornell University, Ithaca, New York, USA

[3]Department of Civil and Environmental Engineering, University of Illinois at Urbana-Champaign, Urbana, Illinois, USA

Correspondence
David S. Kammer, Institute for Building Materials, ETH Zurich, Zurich, Switzerland.
Email: dkammer@ethz.ch

Abstract

We present a 3D hybrid method which combines the finite element method (FEM) and the spectral boundary integral method (SBIM) to model nonlinear problems in unbounded domains. The flexibility of FEM is used to model the complex, heterogeneous, and nonlinear part— such as the dynamic rupture along a fault with near fault plasticity—and the high accuracy and computational efficiency of SBIM is used to simulate the exterior half spaces perfectly truncating all incident waves. The exact truncation allows us to greatly reduce the domain of spatial discretization compared to a traditional FEM approach, leading to considerable savings in computational time and memory requirements. The coupling of FEM and SBIM is achieved by the exchange of traction and displacement boundary conditions at the computationally defined boundary. The method is suited to implementation on massively parallel computers. We validate the developed method by means of a benchmark problem. Three more complex examples with a low velocity fault zone, low velocity off-fault inclusion, and interaction of multiple faults, respectively, demonstrate the capability of the hybrid scheme in solving problems of very large sizes. Finally, we discuss potential applications of the hybrid method for problems in geophysics and engineering.

KEYWORDS

dynamic fracture, earthquake modeling, finite element method, hybrid method, spectral boundary integral method

1 | INTRODUCTION

Earthquakes are a prime example of complex natural processes with far-from-equilibrium nonlinear dynamics at multiple scales. The lack of quantitative data on timescales capturing multiple large earthquake cycles is a fundamental impediment for progress in the field. Physics-based simulations provide the only path for overcoming the lack of data and elucidating the multi-scale dynamics and spatio-temporal patterns that extend the knowledge beyond sporadic case studies and regional statistical laws.

[Correction added on 20 April 2022, after first online publication: CSAL funding statement has been added.]

The multiscale nature of the earthquake phenomena is manifested as follows. Spatially, a moderate-size earthquake typically propagates over tens of kilometers. However, the physical processes governing the rupture propagation operates within a narrow region at the rupture tip, called the process zone, which may not exceed a few millimeters in size if realistic laboratory-based friction parameters are used.[1] Temporally, an earthquake event, where rapid slip occurs, only lasts for few to tens of seconds. However, the time span between successive large earthquakes may be tens to hundreds of years.[2] Thus, there exists approximately a decade of spatial and temporal scales that must be resolved in a target physics-based simulation of earthquakes and aseismic slip. This necessitates innovation in modeling both the fast dynamic rupture with extreme localization and the slow quasi-static slip, during the interseismic period, that exhibits gradual variations. This is a fundamental challenge in earthquake source physics which has been a focus of computational earthquake mechanics over the past four decades.

Historically, numerical methods for simulating earthquakes and aseismic slip may be classified broadly into two categories: boundary-based methods and domain-based methods. The boundary integral formulation enables reducing the spatial dimension of the problem by one, by invoking the representation theorem of linear elastodynamics, transforming 2D problems into 1D and 3D problems into 2D.[3,4] The spectral formulation of the boundary integral equations has been transformative in seismic applications (e.g., Lapusta et al.[2] and references therein). For example, Lapusta et al.[2] derived accurate adaptive time-stepping algorithms and truncation of convolution integrals that enabled, for the first time, the consistent elastodynamic simulation of a long sequence of events combining rapid slip during earthquake ruptures and slow deformation during the interseismic periods. Nonetheless, the method is limited to homogeneous linear elastic bulk. While the method may be applied, in principle, to heterogeneous linear elastic materials, the lack of a closed form representation of the Green's function either inhibits the method from providing a well-defined solution to many problems of interest or makes it less computationally attractive. Furthermore, the superior performance of the spectral approach and its computational efficiency is only possible for planar interfaces. This precludes the representation of non-planar faults or direct incorporation of fault zone complexity (e.g., damage, and shear bands).

On the other hand, numerical methods based on bulk discretization such as the finite difference (FD) and finite element methods have been used in simulating earthquake ruptures since mid-1970s and early 1980s with the pioneering works of Boore et al.,[5] Andrews,[6] Das and Aki,[7] Archuleta and Day,[8] Day,[9] Virieux and Madariaga,[10] and others. These methods are more flexible than the boundary integral approaches in handling heterogeneities, nonlinearities, and fault geometry complexities (see Figure 1A,B). In recent years, highly accurate formulations were introduced, including the spectral finite element,[11-15] the discontinuous Galerkin method,[16-20] and higher-order FD schemes.[21-23] A main computational challenge of these methods is the need to discretize the whole bulk, which increases the computational demand by at least one order of magnitude compared to the boundary integral formulation. Furthermore, the computational domain must be truncated at a sufficient distance from the fault surface such that it would not affect the physical solution. While domain truncation has been achieved by the introduction of several widely-used absorbing boundary conditions such as boundary viscous damping,[24] perfectly matching layers,[25] and infinite elements,[26] these methods have limitations. Specifically, in all these methods, artificial reflections exist to varying degrees and the absorbing surfaces must be taken sufficiently far from the fault surface to ensure solution accuracy. Moreover, attempts to perform cycle simulations using these volume-based methods are rare and have been restricted mainly to the quasi-dynamic limit.[27] This is partially due to the high spatial discretization cost and the lack of a systematic approach to handle both dynamic and quasi-dynamic calculations in the same framework which is required for simulating both earthquake ruptures and interseismic slow deformations. Another challenge in these methods is defining fault loading. Currently, this is done by applying displacement-controlled loading at the far boundaries of the simulation box. This, however, makes the fault stressing rate dependent on where the domain is truncated. This problem is solved approximately in the SBI formulation by loading the fault directly through back-slip.

Both bulk and boundary approaches have their merits and limitations. The limitations are evident in 3D FE simulations where computational complexity grows like the inverse of the element size to the fourth power* rendering high resolution models a computational bottleneck. To that end, this article proposes a new hybrid numerical scheme, for the full three-dimensional elastodynamic problem, that combines the 3D FE method and the 2D SBI method to efficiently model fault zone nonlinearities and heterogeneities with high resolution while capturing large-scale elastodynamic interactions in the bulk. The main idea of the method is to enclose the heterogeneities in a virtual strip that is introduced for computational purposes only (see Figure 1C). This strip is discretized using a volume-based numerical method, chosen

---

*For linear 3D FE simulations, the computational complexity is proportional to the number of elements and time steps $\mathcal{O}(N_1 \times N_2 \times N_3 \times N_t)$. Given that $N_i \propto \Delta x^{-1}$ and $N_t \propto \Delta t^{-1}$, $\Delta t \propto \Delta x$, the computational complexity is $O(\Delta x^{-4})$.
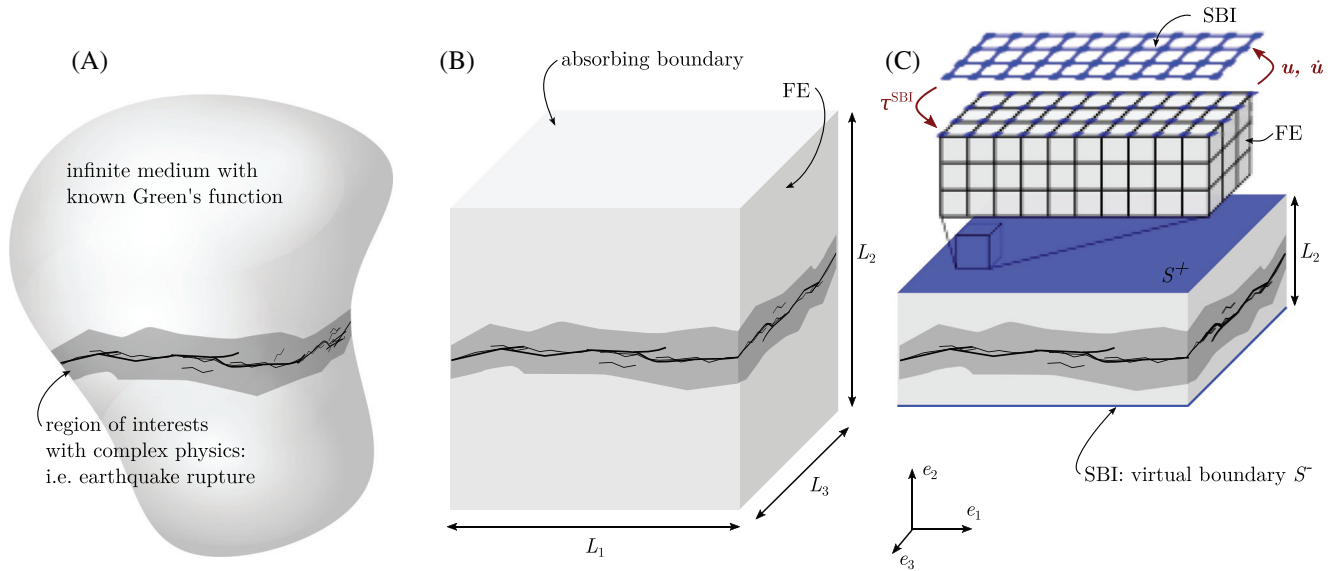
FIGURE 1 Schematic representation of the physical problem (A), it is representation using a domain-based method such as FE (B), and using the hybrid method (C). The hybrid method couples a domain-based method with a boundary-based method, through the communication of nodal traction τ^{SBI}, displacement $\mathbf{u}$, and velocity $\dot{\mathbf{u}}$ at the boundaries of the virtual strip, $S^{\pm}$

here to be the finite element method due to its popularity and flexibility in handling complex geometry and arbitrary bulk heterogeneities. The top and the bottom boundaries of the virtual strip are handled using the independent SBI formulation[4] with matching discretization. The coupling between the two methods is achieved through enforcing continuity of displacement and traction at the virtual boundaries. The current work extends recent work by the authors and their groups over the past few years which first developed the hybrid scheme for the 2D dynamic anti-plane problem combining finite difference and spectral boundary integral methods,[28] and the 2D dynamic in-plane problem using the finite element method for bulk discretization in the hybrid scheme.[29] Prior work has demonstrated the accuracy and computational efficiency of the coupled approach and its potential for modeling dynamic ruptures with high resolution fault zone physics[30] as well as extension to the quasi-dynamic limit and cycle simulations.[31] The current extension to the full three dimensional case represents the culmination of these efforts.

The remainder of this article is organized as follows. In Section 2, we describe the physical model (Section 2.1), and the numerical methods to solve it, which includes the finite-element method (Section 2.2), the spectral boundary integral method (Section 2.3), and their coupling—the hybrid method (Section 2.4). In Section 3, we validate the hybrid method using the benchmark problem TPV3[32] of the Southern California Earthquake Center. Next, we demonstrate the capabilities of the new hybrid method on more complex problems. We consider a low velocity fault zone in Section 4, a low velocity inclusion at a distance from the fault in Section 5, and interacting faults in Section 6. Finally, we discuss the advantages of the hybrid method in terms of computational cost in Section 7 and draw conclusions in Section 8.

2 | METHOD

2.1 | Physical model

We solve the fully dynamic three-dimensional problem of a rupture propagating along a fault embedded in an elastic solid. The conservation of linear momentum within the elastic domain Ω is given by

$$\rho \ddot{u}_i - \frac{\partial \sigma_{ij}}{\partial x_j} - b_i = 0 \quad \text{in } \Omega \tag{1}$$

where ρ is the material density, u_i the displacement vector, with the "dot" being the derivative with respect to time t, σ_{ij} the Cauchy stress tensor, x_j the coordinate vector, and b_i are body forces. Here, for simplicity we assume that b_i are

time independent and satisfy the balance equation for initial stresses. Therefore, incremental stresses, which we consider here, satisfy the equation of motion with $b_i = 0$. Dirichlet boundary conditions are applied on S_u and Neumann boundary conditions are applied on S_T

$$u_i = \bar{u}_i \qquad \text{on } S_u \tag{2}$$

$$\sigma_{ij} n_j = \bar{\tau}_i \qquad \text{on } S_\tau, \tag{3}$$

where n_i is the normal vector to the surface S_τ. Initially, the domain is assumed to be in equilibrium, and, hence, the initial conditions are given by $u_i(0) = u_i^0$ and $\dot{u}_i(0) = 0$. We assume linear elastic material behavior:

$$\sigma_{ij} = \lambda \, \delta_{ij} \varepsilon_{kk} + 2\mu \, \varepsilon_{ij} \tag{4}$$

with the infinitesimal strain tensor $\varepsilon_{ij} = (\partial u_i / \partial x_j + \partial u_j / \partial x_i)/2$ and the Lamé parameters λ, μ describing the elastic properties of the material.

The fault transmits stresses from one half-space to the other through interface tractions. We focus on tangential (friction) interaction and impose non-penetration/non-opening conditions to the normal component of the fault surfaces $S_f^\pm$. The local slip vector, which corresponds to the tangential fault opening vector, is given by

$$\delta_i = R_{ij}(u_j^+ - u_j^-) \quad \text{on } S_f^\pm, \tag{5}$$

where R_{ij} is the global-to-local rotation matrix and $+$ and $-$ indicate the upper and lower fault sides, respectively. Local slip δ is the amplitude of δ_i. The fault is governed by a stick-slip behavior that is described by two states. A sticking section of the fault is described by:

$$\dot{\delta} = 0 \quad \text{and} \quad \tau < \tau^s \tag{6}$$

where $\dot{\delta}$ is slip rate, τ the amplitude of the fault shear traction vector and τ^s the fault strength. A sliding fault section is described by:

$$\dot{\delta} > 0 \quad \text{and} \quad \tau = \tau^s. \tag{7}$$

A constitutive law is applied to model the fault strength evolution. For simplicity, we apply a linear slip-weakening friction law,[33] which is given by:

$$\mu(\delta) = \begin{cases} \mu_s - (\mu_s - \mu_k) \, \delta/\delta_c & \text{for } \delta < \delta_c \\ \mu_k & \text{for } \delta \geq \delta_c \end{cases} \tag{8}$$

where μ_s and μ_k are the static and kinetic friction coefficient, respectively, and δ_c is the characteristic slip length to reach residual strength. The fault strength is then given by $\tau^s = \sigma^n \mu(\delta)$, where σ^n is the normal stress. Other friction laws, such as rate-and-state friction,[34,35] could also be applied in a similar framework, as shown by Kaneko et al.[15] These laws would be suitable for modeling seismic and aseismic periods since they automatically account for strength recovery in the stick phase.

2.2 | Finite element method (FEM)

The finite element method is based on a variational formulation of the governing equation and applies a discretization based on shape functions to find an approximate solution to the physical problem presented in Section 2.1. A detailed description can be found in standard textbooks.[36] The FEM approach transforms the strong form, that is, the governing Equation (1), to the weak form by multiplying it with the test functions $\hat{u}(x)$, integrating it over the domain, and applying Green's identity, which results in:

$$\int_\Omega \rho \ddot{u}_i \, \hat{u}_i \, d\Omega + \int_\Omega \sigma_{ij} \frac{\partial \hat{u}_i}{\partial x_j} d\Omega - \int_{S_\tau} \bar{\tau}_i \, \hat{u}_i \, dS - \int_{S_f} \tau_i \, \hat{u}_i \, dS = 0. \tag{9}$$

Test functions are chosen smooth enough, such that all steps are well defined and vanish on the Dirichlet boundary. By choosing suitable interpolation functions, $N_I(x_J) = \delta_{IJ}$, and test function $\hat{u}(x) = \sum_I N_I(x) u_I(t)$, where the subscript I represent the node index, $u_I(t)$ becomes the nodal displacements. Using this standard FE approach, the weak form can be expressed as the following matrix equation

$$\mathbf{M\ddot{u} + Ku - f - B\tau = 0} \tag{10}$$

where $\mathbf{\ddot{u}}$ denotes the second time derivative of the displacement vector, $\mathbf{M}$ and $\mathbf{K}$ are the mass and stiffness matrix, respectively, $\mathbf{B}$ is a fault rotation-area matrix, τ is the fault traction vector, and $\mathbf{f}$ is the force vector from Neumann boundary conditions.

We apply an explicit central-difference time integration formulation with a predictor-corrector formulation. The step-by-step procedure follows:

$$\mathbf{\dot{u}}_{t+1}^{pred} = \mathbf{\dot{u}}_t + \Delta t \, \mathbf{\ddot{u}}_t \tag{11}$$

$$\mathbf{u}_{t+1} = \mathbf{u}_t + \Delta t \, \mathbf{\dot{u}}_{t+1}^{pred} \tag{12}$$

$$\Delta\mathbf{\ddot{u}} = (-\mathbf{Ku}_{t+1} + \mathbf{f} + \mathbf{B\tau}_{t+1})\,\mathbf{M}^{-1} - \mathbf{\ddot{u}}_t \tag{13}$$

$$\mathbf{\dot{u}}_{t+1} = \mathbf{\dot{u}}_{t+1}^{pred} + \frac{1}{2}\Delta t \, \Delta\mathbf{\ddot{u}} \tag{14}$$

$$t = t + \Delta t \tag{15}$$

where the subscript indicates the time step and Δt is the current incremental time step, which is required to satisfy the Courant–Friedrichs–Lewy (CFL) condition.[37] We apply a lumped mass matrix, which simplifies the computation of the inverse mass matrix and reduces computational cost of the time-integration scheme. The fault rotation matrix is scaled by the fault-surface area associated with each fault-split-node and thus transforms the fault traction vector τ to a nodal force vector.

The fault traction vector τ_{t+1} in Equation (13) is computed by a forward Lagrange multiplier method,[38] which uses a prediction procedure to pre-compute the slip rate for the next time step. A similar approach was applied in spectral-element simulations.[15] We denote a fault discontinuity as $[|A|] = (A^+ - A^-)$ where superscript $+$ and $-$ indicate the upper and lower fault sides, respectively. The predicted slip rate during the next time step if no fault tractions were applied is given by

$$[|\mathbf{\dot{u}}_{t+3/2}|] = [|\mathbf{\dot{u}}_{t+1}^{pred} - \frac{\Delta t}{2}\mathbf{\ddot{u}}_t - \Delta t \, \mathbf{M}^{-1}(\mathbf{Ku}_{t+1} - \mathbf{f})\,|]. \tag{16}$$

We use the slip-rate predictor $[|\mathbf{\dot{u}}_{t+3/2}|]$ because the no-slip-rate condition $[|\mathbf{\dot{u}}_{t+3/2}|] = 0$ will ensure that the interface remains stuck and hence $[|\mathbf{u}_{t+2}|] = [|\mathbf{u}_{t+1}|]$. Using Equation 16, we can compute the traction required to maintain slip and impose stick condition on the fault by

$$\tilde{\tau}_{t+1} = \frac{1}{2}\mathbf{Z}[|\mathbf{\dot{u}}_{t+3/2}|], \tag{17}$$

where $\mathbf{Z}$ is the fault impedance matrix given by $\mathbf{Z}^{-1} = \Delta t \left((\mathbf{M}^+)^{-1}\mathbf{B}^+ + (\mathbf{M}^-)^{-1}\mathbf{B}^-\right)/2$ and the following fault traction balance was applied $\tau = -\tau^+ = \tau^-$. The actual fault traction is computed by applying the stick-slip conditions given by Equations (6) and (7):

$$\tau_{t+1} = \begin{cases} \tilde{\tau}_{t+1} & \text{if} \quad \tilde{\tau}_{t+1} < \tau_{t+1}^s \quad \text{(stick)} \\ \tau_{t+1}^s & \text{otherwise} \quad\quad \text{(slip)} \end{cases} \tag{18}$$

where τ_{t+1} and $\tilde{\tau}_{t+1}$ are individual entries in τ_{t+1} and $\tilde{\tau}_{t+1}$, respectively, and τ_{t+1}^s is the fault strength at each split-node (node indicator is omitted for simplicity) and is governed by Equation (8).

2.3 | Spectral boundary integral method (SBIM)

Boundary integral methods have the advantage of modeling the wave propagation problem in the entire domain Ω by using a spatio-temporal integral relationship between the displacements and the tractions along the boundary of the domain $\partial\Omega$. The advantage lies in reduced computational cost and increased accuracy with respect to a finite-element or finite-difference method. For these reasons, boundary integral methods have been used extensively since the mid-1980s to study crack propagation problems.[3,39-48]

Consider the displacements and tractions at the boundary of an semi-infinite half space with the boundary lying on the e_1, e_3 plane and the domain being infinite in the e_2 direction. Following the process described in Geubelle and Rice,[4] the elastodynamic response of a 3D elastic half space is given by

$$\tau_i^{SBI}(x_1, x_3, t) = \tau_i^\infty(x_1, x_3, t) - \eta_{ij}\frac{\mu}{c_s}\dot{u}_j(x_1, x_3, t) + s_i(x_1, x_3, t), \tag{19}$$

where η_{ij} is a diagonal matrix with $\eta_{11} = \eta_{33} = 1$ and $\eta_{22} = c_s/c_p$. c_p and c_s are the longitudinal and shear wave speeds of the material, respectively. Equation (19) states that the traction at the surface of the half space, τ_i^{SBI}, equals the far field traction, τ_i^∞, plus a "radiation damping" term, $\eta_{ij}\frac{\mu}{c_s}\dot{u}_j^\pm$, and a spatio-temporal integral term s_i. In this formulation, the elastodynamic response is separated between local and nonlocal contributions. s_i represents the nonlocal elastodynamic long-range interaction between different parts of the surface, and the local effect $\eta_{ij}\frac{\mu}{c_s}\dot{u}_j$ represents wave radiation from the surface.

We use the spectral approach[49] for computing s_i, which involves a Fourier transform in space and a convolutions in time, where the displacement history is convolved with the elastodynamic kernels H. The Fourier representation of displacements and long-range interaction term is defined as follows:

$$[u_j^\pm(x_1, x_3, t), s_j(x_1, x_3, t)] = [\hat{u}_j^\pm(t; k, m), \hat{s}_j(t; k, m)]\exp\left(i(kx_1 + mx_3)\right), \tag{20}$$

where the wave number vector is $\mathbf{q} = (k, m)$.

The spatio-temporal integral term in the Fourier space becomes:

$$\begin{Bmatrix}\hat{s}_1^\pm(t; k, m) \\ \hat{s}_2^\pm(t; k, m) \\ \hat{s}_3^\pm(t; k, m)\end{Bmatrix} = -i\mu^\pm(2 - \eta^\pm)\begin{pmatrix}0 & -k & 0 \\ k & 0 & m \\ 0 & -m & 0\end{pmatrix}\begin{Bmatrix}\hat{u}_1^\pm(t; k, m) \\ \hat{u}_2^\pm(t; k, m) \\ \hat{u}_3^\pm(t; k, m)\end{Bmatrix} \tag{21}$$

$$-\mu^\pm|q|\int_0^t\left[i\frac{H_{12}(|q|c_s^\pm t')}{|q|}\begin{pmatrix}0 & -k & 0 \\ k & 0 & m \\ 0 & -m & 0\end{pmatrix} \pm H_{22}(|q|c_s^\pm t')\begin{pmatrix}0 & 0 & 0 \\ 0 & 1 & 0 \\ 0 & 0 & 0\end{pmatrix}\right. \tag{22}$$

$$\left.\pm\frac{H_{11}(|q|c_s^\pm t')}{q^2}\begin{pmatrix}k^2 & 0 & km \\ 0 & 0 & 0 \\ km & 0 & m^2\end{pmatrix} \pm \frac{H_{33}(|q|c_s^\pm t')}{q^2}\begin{pmatrix}m^2 & 0 & -km \\ 0 & 0 & 0 \\ -km & 0 & k^2\end{pmatrix}\right] \tag{23}$$

$$\times\begin{Bmatrix}\hat{u}_1^\pm(t - t'; k, m) \\ \hat{u}_2^\pm(t - t'; k, m) \\ \hat{u}_3^\pm(t - t'; k, m)\end{Bmatrix}|q|c_s^\pm dt', \tag{24}$$

where $|q| = \sqrt{k^2 + m^2}$ and $\eta = c_p/c_s$. The in-plane convolution kernels are defined by the following inverse Laplace transforms:

$$H_{11}(t) = \mathfrak{L}^{-1}\left[\frac{\tilde{p}^2\sqrt{\tilde{p}^2 + \eta^2}}{\sqrt{\tilde{p}^2 + \eta^2}\sqrt{\tilde{p}^2 + 1} - \eta} - \tilde{p}\right],$$

$$H_{12}(t) = \mathfrak{L}^{-1}\left[\frac{-\eta\tilde{p}^2}{\sqrt{\tilde{p}^2+\eta^2}\sqrt{\tilde{p}^2+1}-\eta}+\eta\right],$$

$$H_{22}(t) = \mathfrak{L}^{-1}\left[\frac{\eta\tilde{p}^2\sqrt{\tilde{p}^2+1}}{\sqrt{\tilde{p}^2+\eta^2}\sqrt{\tilde{p}^2+1}-\eta}-\eta\tilde{p}\right], \tag{25}$$

where $\tilde{p} = p/|q|c_s$ is the non-dimensional Laplace transform variable. The inverse Laplace transform is

$$H(t) = \mathfrak{L}^{-1}[h(\tilde{p})] = \frac{1}{2\pi i}\int_{\gamma-i\infty}^{\gamma+i\infty}\exp(\tilde{p}t)h(\tilde{p})\mathrm{d}\tilde{p}, \tag{26}$$

which can be evaluated numerically, for example, using the approach by de Hoog et al.[50] On the other hand, the out-of-plane convolution kernel has a closed form solution

$$H_{33}(t) = J_1(t)/t, \tag{27}$$

where $J_1(t)$ is the Bessel function.

In a classical SBIM, Equation (19) is integrated in time explicitly by first solving for $\dot{u}$ and then computing the displacement at the next time step $u_i(t+\Delta t) = u_i(t) + \Delta t\,\dot{u}_i(t)$. The time step is required to satisfy the following CFL condition:[49] $\Delta t < 0.35\Delta x/c_s$.

2.4 | Hybrid FEM-SBIM method

The hybrid method consists in coupling the FEM and the SBIM at the boundaries $S^\pm$, where the FE-domain is truncated (see Figure 1C). However, instead of FEM, one could use any other domain-based method. In the hybrid method, all nonlinear behavior, such as multi-physics processes, fault roughness, diffuse damage, material nonlinearities, and local heterogeneity need to be confined within a virtual strip, which we introduce for computational purposes only (see Figure 1). Beyond this strip, it is assumed that the material is homogeneous and linear-elastic. Thus, it may be modeled as a top and bottom half spaces coupled to the strip. The width of the virtual strip depends on the problem being solved and it can be adjusted to include all complexities and nonlinearities. At $S^\pm$, which we refer to as the virtual boundary, we apply an exact elastodynamic transparent boundary condition using the SBIM, which accounts for wave propagation in the infinite half-space beyond the FE truncation. At each time step of a simulation, the two methods exchange traction and displacements boundary conditions along the virtual boundaries.

Depending on the FE scheme, Neumann or Dirichlet boundary conditions might be more suitable for the virtual boundary. For example, Dirichlet boundary conditions might result in a more stable algorithm. Here, we present the Neumann approach (for the Dirichlet approach please refer to Ma et al.[29]). We impose continuity condition at the boundaries $S^\pm$, which results in the FE force $\mathbf{f}$ being equal to the SBI traction τ^{SBI} multiplied by a rotation-area matrix $\mathbf{B}^{\mathbf{SBI}}$. For appropriate accuracy of the wave absorption algorithm, we use a staggered approach in which FEM and SBIM share nodes at the virtual boundary (see Figure 1C). Thus, the continuity condition is enforced directly on nodal values, without relying on interpolation. Therefore, the spatial discretization at $S^\pm$ must be a regular quadrangular grid and each FE-node on $S^\pm$ has a corresponding SBI-node at the exact same location.

Because of continuity at $S^\pm$, displacement, velocity, and traction of SBIM and FEM must coincide. Therefore, the coupling needs to involve the SBI Equation (19), which relates traction to the history of displacement and current velocity, and the FE weak form Equation (10), which relates displacement and applied force to acceleration.

The Neumann approach consists in solving the SBI relation, Equation (19), by using the displacement and velocity computed from the FEM. The resulting traction represents the response of the truncated half space and is then applied as a Neumann boundary condition in the FEM. A time step of the hybrid method is computed as follows:

1. FE predict velocity Equation (11) and compute explicit time integration Equation (12).
2. Copy $\mathbf{u}_{t+1}$ and $\dot{\mathbf{u}}_{t+1}^{pred}$ from FE to SBI.
3. SBI compute response of half space, τ^{SBI}, for given displacement history $u(x_1,x_3,t)$ and current velocity prediction $\dot{u}_{t+1}^{pred}$ Equation (19).
4. Apply SBI interface traction as Neumann boundary condition in FE: $\mathbf{f} = \mathbf{B}^{\mathbf{SBI}}\tau^{\mathrm{SBI}}$.

5. FE compute friction traction τ_{t+1} using Equation (18).
6. FE compute acceleration increment Equation (13).
7. FE correct velocity Equation (14).

Given the periodicity of the SBI-formulation, the side faces of the virtual strip are also subjected to periodic boundary conditions: $u_i(0, x_2, x_3) = u_i(L_1, x_2, x_3)$ and $u_i(x_1, x_2, 0) = u_i(x_1, x_2, L_3)$. Further, the time step of the hybrid scheme needs to satisfy the CFL condition of both FEM and SBIM and the time step must be the same.

Note that in the suggested hybrid scheme, the SBI evaluation of the time integration of the convolution term and the radiation damping term are computed using the predicted velocity (without correction). This approach is stable because it corresponds to the SBI integration scheme, where the velocity used for the time integration depends on the previous time step only, see Section 2.3.

Alternative coupling methods, for example, Lagrange multiplier, could also be applied. However, as we will show in Section 3, the simple staggered approach proposed here provides excellent accuracy and is optimal in terms of computational efficiency. Further, in the finite-element domain, we apply 8-node linear hexagonal elements in a regular mesh in all presented problems.

The hybrid scheme is conceptually simple. However, the challenges lie in the implementation within a distributed memory parallelism framework, where the FEM mesh is scattered to different processes. Here, we couple an open-source FEM library, *akantu*[51] with an in-house, open-source SBIM library called *uguca*.[52] In order to avoid any changes of the FEM code we implemented a new class in our SBIM code, which creates the interface between the distributed FEM mesh and the non-distributed SBIM mesh. In this way, one can easily implement the hybrid method with any FEM library.

3 | BENCHMARK PROBLEM TPV3: EARTHQUAKE RUPTURE IN UNBOUNDED HOMOGENEOUS DOMAIN

3.1 | Setup

We verify the hybrid method with the benchmark problem TPV3 from the SCEC Dynamic Rupture Validation exercises (https://strike.scec.org/cvws/). The problem considers a planar fault, governed by linear slip-weakening friction, embedded in a homogeneous linear elastic bulk (see Figure 2A). The elastic bulk has a density of $\rho = 2670$ kg/m^3, pressure wave speed $c_p = 6000$ m/s, and shear wave speed $c_s = 3464$ m/s. The friction properties are uniform and characterized by $\mu_s = 0.677$, $\mu_k = 0.525$, and $d_c = 0.4$ m. A uniform background shear, $\tau_0 = 70$ MPa, and normal stress, $\sigma_0 = 120$ MPa, are applied. The rupture is nucleated at the center of the fault over a square patch of size a^2 by instantaneously increasing the shear stress to a value higher than the static friction. After nucleation, the rupture quickly propagates across the entire fault. The fault is bounded by a locked region (depicted in dark gray in Figure 2) where the rupture cannot propagate due to high fault strength.

Note that this problem does not present any off-fault non-linearities and the fault is planar. Hence, the hybrid method is not required for this particular problem, which could be solved solely by the SBIM. However, we use this problem to verify the hybrid method by comparing the results with the reference solution of the SBIM. Additional examples, which do include non-linearities that require the hybrid method, will be presented in the following sections.

Additionally, in this example (as well as in Sections 4 and 5) the fault (i.e., the 13 plane) represents a symmetry plane. The implications of this are twofold: (i) the normal stress on the fault remains constant throughout the simulation and so do the peak and residual friction strengths (ii) there is no need of explicitly modeling the bottom half space of the simulation domain (i.e., $x_2 < 0$)), which is taken into account for when applying the frictional traction on the fault by enforcing $[|u_2|] = 0$ and $\sigma_{22} = const$. Note that, by applying the hybrid method, we model the entire top (i.e., $x_2 > 0$) half space. However, there are two additional symmetry planes: the 12 plane and the 23 plane. Thus, the FE computational domain could be further reduced by using the appropriate boundary conditions.

3.2 | Results

We present the results of the hybrid method with a virtual strip width $L_2 = 4\Delta x$ (see Figure 2B) and compare it with the reference solution. For both methods we use the same spatial discretization with $\Delta x = 50$ m. Rupture front position

(see Figure 3A), and stress and slip time history at four stations (see Figure 3B) show excellent agreement between the hybrid method and the SBIM. Slight offset in rupture arrival times (see Station C and D in Figure 3B), are caused by minor differences in spatial discretization of the nucleation patch and locked region between SBI and Hybrid method. Figure 4 shows the velocity field on one quadrant of the virtual strip. The rupture front is characterized by an abrupt change from peak to residual strength. The excellent agreement with the reference solution (Figure 3) demonstrates that the elastodynamic boundary condition enforced on the planes $S^{\pm}$ does not cause any artificial wave reflection even though the virtual strip is extremely thin.

We perform a mesh convergence study of the hybrid method. First, we compute the ℓ_2 norm error on the displacement **u** and on shear stress σ_{12} and σ_{13} at a given time $t = 3$ s. The ℓ_2 norm error of **u** is defined as

$$\left\| u_i(\mathbf{x}) - u_i^{ref}(\mathbf{x}) \right\|_2 = \sqrt{\int_{\Omega} \sum_{i=1}^{3} \left(u_i(\mathbf{x}) - u_i^{ref}(\mathbf{x}) \right)^2 d\Omega} \tag{28}$$

The reference solution, u_i^{ref}, is solved using the hybrid method with a very fine mesh ($\Delta x = 25$ m). The results show that the error converges with order between 1 and 2, depending on Δx and on the considered field (see Figure 5A). The ℓ_2 norm error of σ_{ij} is computed analog to Equation (28) but without the sum over dimensions i. The hybrid method combines linear finite elements with a higher precision spectral boundary method. Therefore, the convergence rate of the hybrid method corresponds to the rate of the least accurate of the methods it combines, that is, the linear finite element
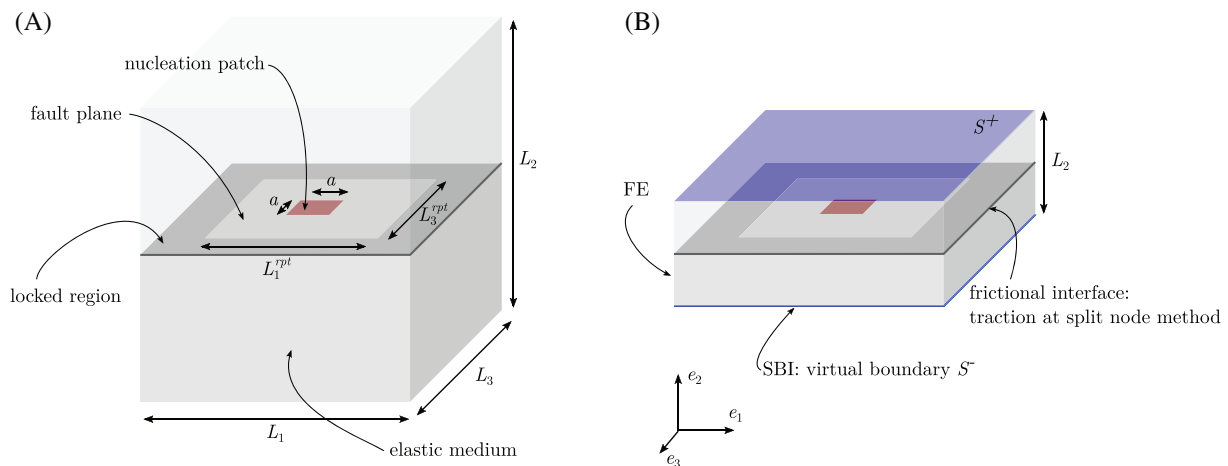

FIGURE 2 Setup of benchmark problem TPV3. (A) Earthquake rupture in unbounded domain with nucleation over square region of size $a = 3$ km and fault regions of size $L_1^{rpt} = 30$ km and $L_3^{rpt} = 15$ km, while $L_1/L_1^{rpt} = L_3/L_3^{rpt} = 1.5$. (B) Hybrid setup: FE domain with SBI as elastodynamic boundary condition
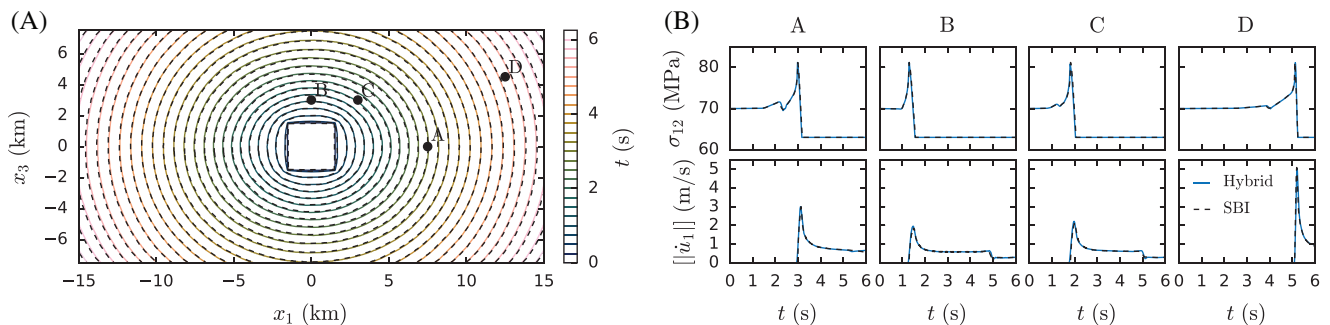

FIGURE 3 Benchmark problem TPV3 solved using hybrid method (multicolor lines) and using the SBIM (dashed black lines) with $\Delta x = 50$ m (2.4M FE-Degrees-Of-Freedom (DOF) and 1.2M SBI-DOF). (A) Contour of rupture front position each 0.5 s. (B) Fault shear stress, σ_{12}, and slip rate, $\dot{u}_1$, at three stations A, B, C, and D with position shown in (A)
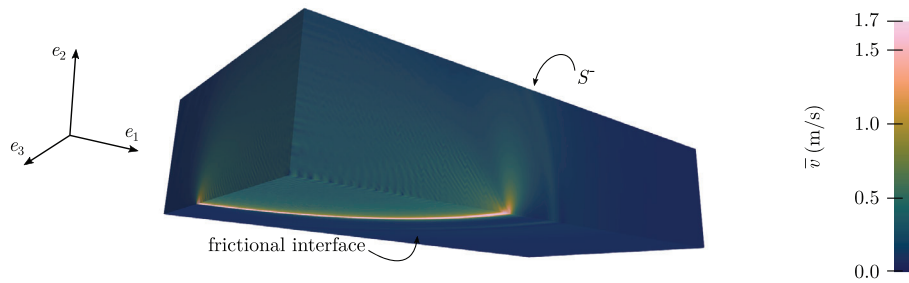
FIGURE 4 Benchmark problem TPV3 solved using hybrid method. Velocity magnitude field, $\bar{v}$, at $t = 3.4$ s. For better visualization we applied a much thicker virtual strip, that is, $L_2 = 10$ km instead of $L_2 = 0.2$ km as applied for simulations shown in Figure 3. Here, only 1/4 of the virtual strip is shown, following the symmetry axes
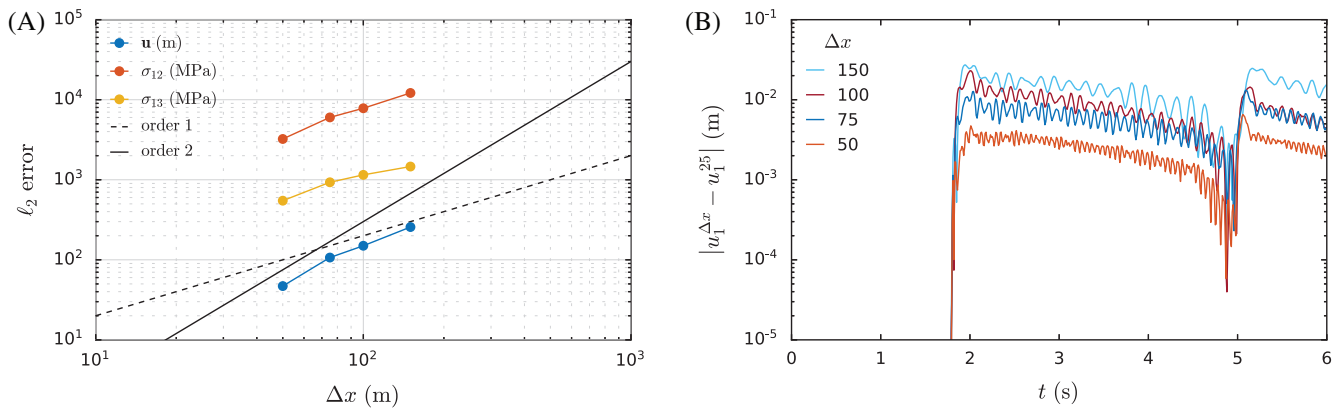

FIGURE 5 Mesh convergence study on benchmark problem TPV3 solved with hybrid method (A) ℓ_2 error of displacement $\mathbf{u}$ and shear stress σ_{12} and σ_{13} as function of mesh size Δx computed over the entire fault at $t = 3$ s. (B) Absolute error of displacement u_1 as function of time at station C

method. Hence, the hybrid method does not loose any accuracy compared to a fully FE model. Here, since we are using linear interpolation functions in our FEM, one would expect order 2 convergence. However, in our problem the solution has geometric structures such as the shape of the propagating rupture front and the process zone size which evolve in time. Finer meshes represent these geometric structures and their temporal evolution more accurately and approach convergence order 2, while coarser meshes have lower order of convergence.

Second, since we are dealing with a dynamic problem, we show the temporal evolution of the absolute error on the displacement u_1 at station C (see Figure 5B). The error is initially zero because neither elastic waves nor rupture have reached the station yet. At $t \approx 1.8$ s, the rupture reaches the station (see also Figure 3B) and hence the error increases rapidly. It then remains approximately constant while the fault continues to slide until reflected waves from the boundary between rupture region and locked region (not the virtual boundary) reach the station. At this point, we notice a temporary drop in the error before it increases again to the same level of error observed before. Overall, we find that the error remains mostly constant over the duration of the simulation and decreases with mesh refinement.

Even though this benchmark problem is linear elastic and does not necessitate the use of the hybrid method, it illustrates its capability of efficiently and accurately truncating elastic waves in the vicinity of the fault with no artificial reflections from the virtual boundaries, $S^{\pm}$, which were only two elements away from the fault. In more complex scenarios, this virtual strip might need to be larger in order to fully describe the source of non-linearities or heterogeneity. Nevertheless, this efficient near-field truncation algorithm enables us to decrease the domain of finite-element discretization, compared to a fully FEM model, and apply a volumetric mesh only in a narrow strip around the fault, which results in considerable savings in terms of both computational time and memory, as we will discuss further in Section 7.

4 | EARTHQUAKE RUPTURE WITH LVFZ: PULSE-LIKE BEHAVIOR

4.1 | Setup

The previous example was a benchmark problem and could have been solved by a boundary-element approach without any discretization of the bulk. Hence, the hybrid method was not required. In the following, we will consider more complex problems, which require volumetric discretization. First, we consider a slip-weakening fault with a low velocity fault zone (LVFZ). LVFZ are found in most mature faults, where the near fault rock is considerably damaged and, as a consequence, has a reduced wave speed ranging from 20% to 60% with respect to the host rock.[53-57] In 2D setups, when the reduction is high enough, the rupture behaves like a pulse. The results presented here will confirm this behavior on a 3D setup.

We consider a velocity reduction of 20% with respect to the surrounding host rock, which has the same elastic properties as in Section 3. The fault geometry is given in Figure 6, and is governed by linear slip-weakening friction with $\mu_s = 0.677$, $\mu_k = 0.564$, and $d_c = 0.2$ m. The fault is subjected by a uniform background shear $\tau^0 = 27.5$ MPa and normal $\sigma^0 = 44$ MPa stress. We nucleate the fault rupture over a square region of size a^2 by instantaneously applying a loading traction of 31 MPa, which locally exceeds the peak friction strength.

4.2 | Results

As a result of the nucleation procedure, the rupture front quickly propagates radially and eventually spans the entire fault (see Figure 7). When a dynamic rupture propagates, it radiates elastic waves, which are then reflected at the boundary of the LVFZ.[57] Depending on the incident angle, the reflected wave can have an inverted polarization and cause unloading of the fault and generate a slip pulse. This effect is also observed in our 3D simulations and is shown in Figure 7B, station C, and in Figure 9. The reflected wave causes the rupture to split into a pulse-like rupture, followed by a crack-like rupture. Reflected waves also cause perturbation of the rupture front, which is not circular anymore (see Figure 7A at $x_1 \approx \pm 25$ km).

Since this problem cannot be solved with the SBI method, we validate the results of the hybrid method by varying the width of the virtual strip, L_2. The solution is independent on the location of the elastodynamic boundary condition (see Figure 7), which can be placed at or beyond the boundary between the stiff and compliant regions, $L_2 \geq L_{FZ}$. When computing the error between solutions with different L_2, minor differences become visible (see Figure 8).

The rapid acceleration and deceleration of a slip pulse are a source of high frequencies (see Figure 7B station C) and cause oscillations in slip velocity, trailing the rupture front (see Figure 9). These oscillations do not affect the rupture
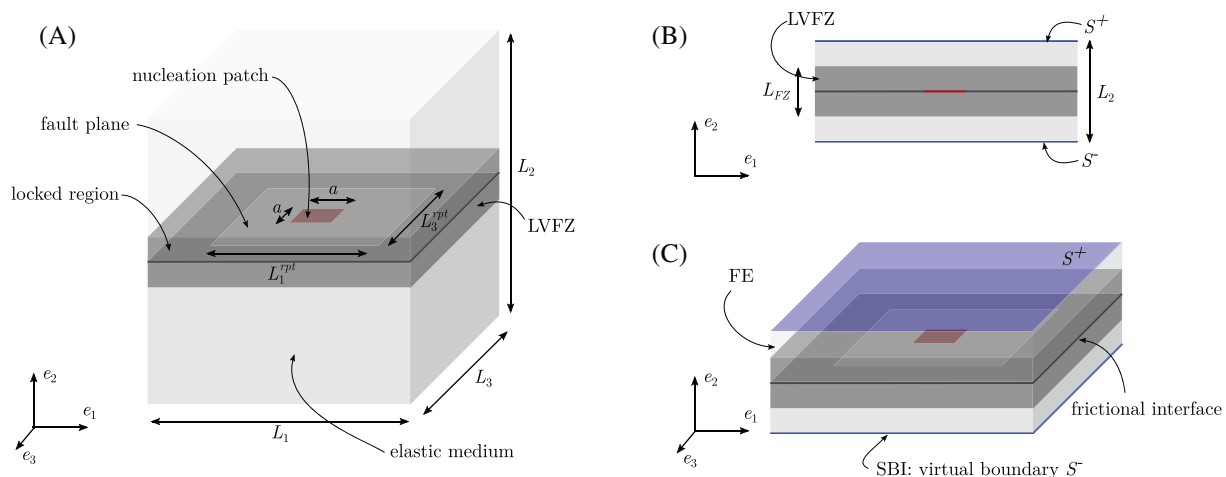

FIGURE 6 Setup of example earthquake rupture in unbounded domain with LVFZ. (A) Fault plane geometry and nucleation patch are analogous to the previous example but with a larger size: $L_1^{rpt} = 60$ km, $L_3^{rpt} = 30$ km, and $a = 3.2$ km. The fault zone region surrounding the fault is more compliant and presents a thickness of $L_{FZ} = 1.6$ km. (B) Hybrid setup: FE virtual strip with $L_2 = 2$ km and with SBI as elastodynamic boundary condition
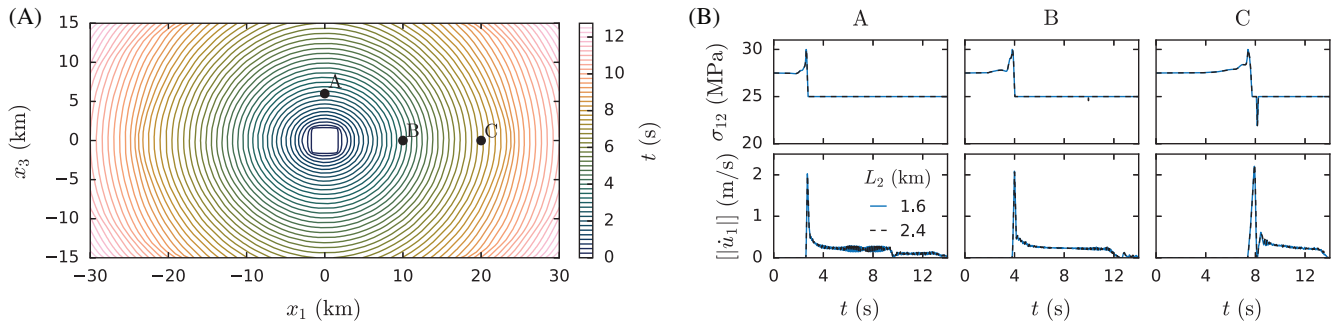
FIGURE 7 LVFZ setup solved using hybrid method with $\Delta x = 100$ m (12M-18M FE-DOF and 1.2M SBI-DOF). (A) Contour of rupture front position each 0.5 s. (B) Fault shear stress, σ_{12}, and slip rate, $[|\dot{u}_1|]$ at three stations A, B, and C with position shown in (A). At station C the rupture has split into a slip-pulse followed by a crack-like rupture. Two solutions with different L_2 are shown (see Figure 8 for quantitative comparison)
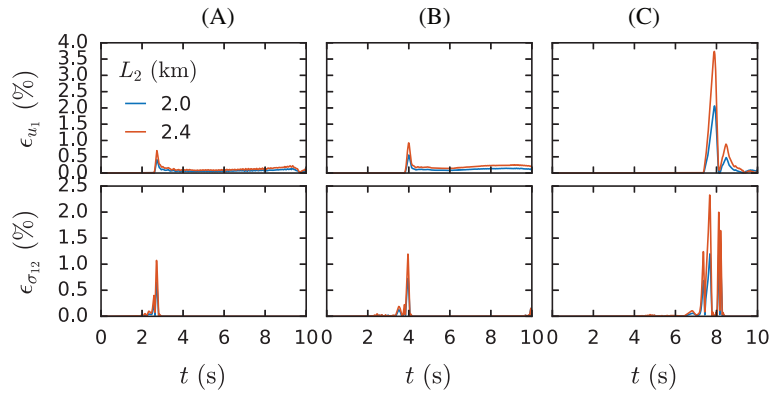

FIGURE 8 Error of hybrid method with $\Delta x = 100$ m and different virtual strip widths L_2 using LVFZ setup. Normalized error, $\epsilon_a = |a(x) - a^{ref}(x)| / \|a^{ref}(x)\|_\infty$ is computed on the displacement field at stations A, B, and C (defined in Figure 7). The error is computed on u_1 and σ_{12}. The reference solutions is a simulation with $L_2 = L_{FZ} = 1.6$ km (i.e., the virtual boundary corresponds to the boundary between stiff and compliant material). Increasing error with L_2 is expected since accuracy of SBI is superior than FE
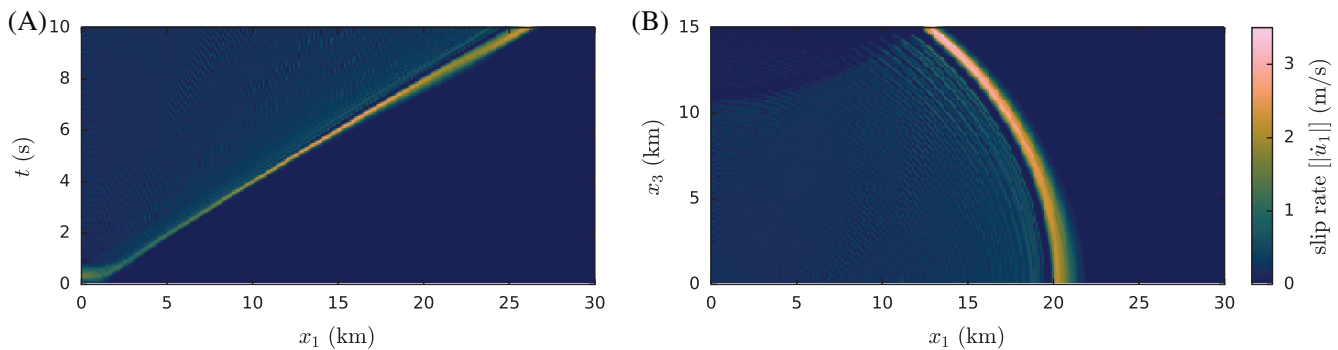

FIGURE 9 Pulse like rupture induced by LVFZ. (A) Space-time diagram of slip rate $[|\dot{u}_1|]$ along the symmetry axis $x_3 = 0$ km. At $t \approx 5$ s, the rupture splits into a slip-pulse, followed by a crack-like rupture. (B) Slip $[|\dot{u}_1|]$ at $t = 8$ s shows the spatial extent of the pulse-like and crack-like rupture

propagation and could be decreased by using regularized friction laws[58] or numerical damping, which are not used here.

5 | EARTHQUAKE RUPTURE IN A HETEROGENEOUS MEDIUM: SUPERSHEAR TRANSITION

5.1 | Setup

The second showcase example, presented in this section, is similar to the previous example but with the more compliant material being the one at a distance from the fault. We consider a slip-weakening fault with an off-fault low velocity zone. This case could occur when a fault ruptures and interacts with the LVFZ of a nearby mature fault.[53,57] We use the same geometry, friction and elastic properties, and nucleation procedure as in Section 4 but consider the fault to be embedded in the reference material, while beyond a distance $L^{FZ}/2$ from the fault plane the material has a 20% velocity reduction.

5.2 | Results

Similar as in the LVFZ setup of Section 4, elastic waves are reflected at the boundary of the low velocity inclusion and affect the shear stress at the interface. However, the reflected waves have the same polarity as the incident ones and, hence, increase the shear stress in front of the propagating rupture front (see Figure 10B). This increasing shear stress peak eventually causes the rupture to transition from subRayleigh to supershear velocities (see Figure 10A and Figure 11). SubRayleigh propagation occurs when the rupture speed is lower than the Rayleigh wave speed, $c_R \approx 0.9c_s$, and can be observed at stations A and B in Figure 10. Supershear propagation, however, refers to ruptures propagating faster than c_s and their speed can approach the limiting speed, c_p.[59,60] In our simulations, supershear rupture occurs within the domain surrounding station C in Figure 10A.

In this 3D simulation, we observe a supershear transition through the Burridge–Andrews mechanism,[6,61] where a shear stress peak in front of the existing crack nucleates the supershear rupture (see Figure 10B, station C and Figure 11). In contrast to 2D setups,[53,57] the extent of the supershear rupture is confined to a triangular shaped region, which surrounds station C. Additionally, the transition occurs progressively: first at $x_3 = 0$ km at $t \approx 7$ s, then it expands towards the $\pm e_3$ direction, and finally, at $t \approx 12$ s it spans the entire seismogenic depth.

This example illustrates the ability of the hybrid method of successfully truncating the shear Mach front, radiated from the supershear rupture, without artificial reflections. Hence, the virtual boundary $S^{\pm}$ can be as close as the boundary between the stiff and the compliant materials. As in the previous problem, we validate the results of the hybrid method by varying the width of the virtual strip, L_2. The solution is found to be independent on L_2, given that $L_2 \geq L_{FZ}$.
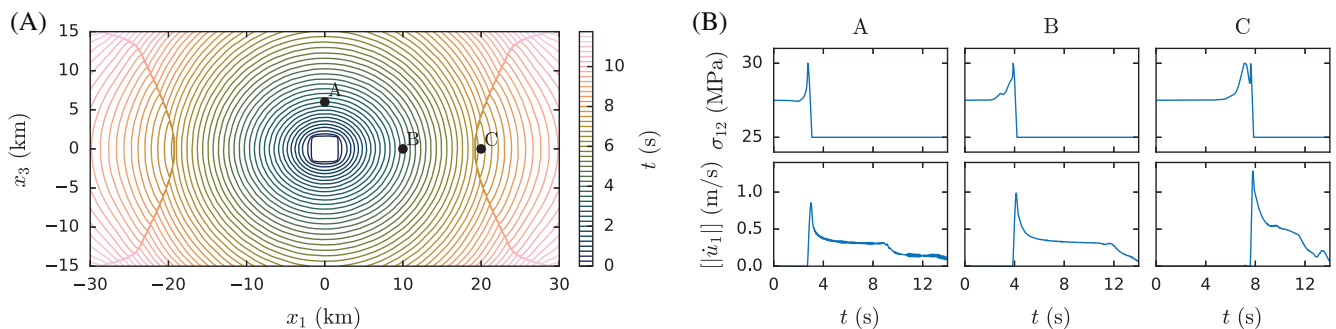

FIGURE 10 Off-fault low velocity zone setup solved using hybrid method with $\Delta x = 100$ m (12M FE-DOF and 1.2M SBI-DOF). (A) Contour of rupture front position each 0.5 s. Widely spaced contour lines represent supershear propagation region. (B) Fault shear stress, σ_{12}, and slip rate, $[|\dot{u}_1|]$ at three stations A, B, and C with position shown in (A)

6 | EARTHQUAKE RUPTURE WITH STEP-OVER FAULTS

6.1 | Setup

Finally, we present an example of interaction between nearby faults, that is, two fracture planes side-by-side. We consider a dilational step-over geometry with a system of two faults that overlap each other (see Figure 12). The dilational step-over implies that the location of the secondary fault with respect to the primary one is such that the rupture propagation on the primary fault will cause a temporary reduction in normal stress. The faults have uniform friction properties, $\mu_s = 0.677$, $\mu_k = 0.373$, and $d_c = 0.5$ m, except on the top 1 km of the seismogenic zone, where a slip-strengthening condition is imposed. At the bottom, that is, $x_3 < L_3^{rpt}$, we consider a no slip boundary condition and the nucleation is achieved by an instantaneous reduction of the friction strength over a region of size $a \times L_3^{rpt}$ to it is kinetic value. This setup is analogous to a recent study by Bai and Ampuero.[62] The elastic properties are the same as in Section 3. We choose a seismogenic depth, $L_3^{rpt} = 10$ km and uniform background shear $\tau_0 = 71.2$ MPa and normal stress $\sigma_0 = 150$ MPa. Hence, the strength ratio is $S = (\mu_s \sigma_0 - \tau_0)/(\tau_0 - \mu_k \sigma_0) = 1.75$, and the condition for the rupture to jump from one fault to the adjacent one is satisfied.[62]
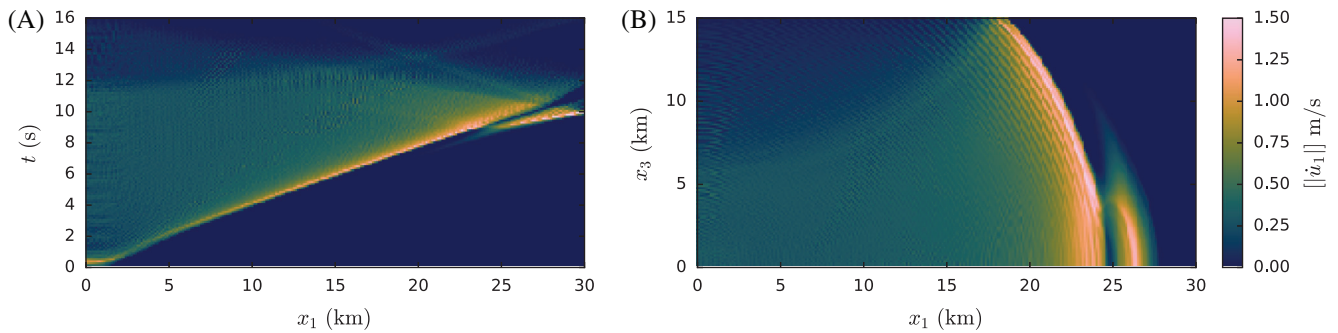

FIGURE 11 Supershear transition induced by off-fault low velocity zone. (A) Space-time diagram of slip rate $[|\dot{u}_1|]$ along the symmetry axis $x_3 = 0$ km. The rupture transitions to supershear at $x_1 \approx 24$ km. (B) Slip rate at $t = 9.25$ s shows the spatial extent of the supershear rupture, just after the transition has initiated
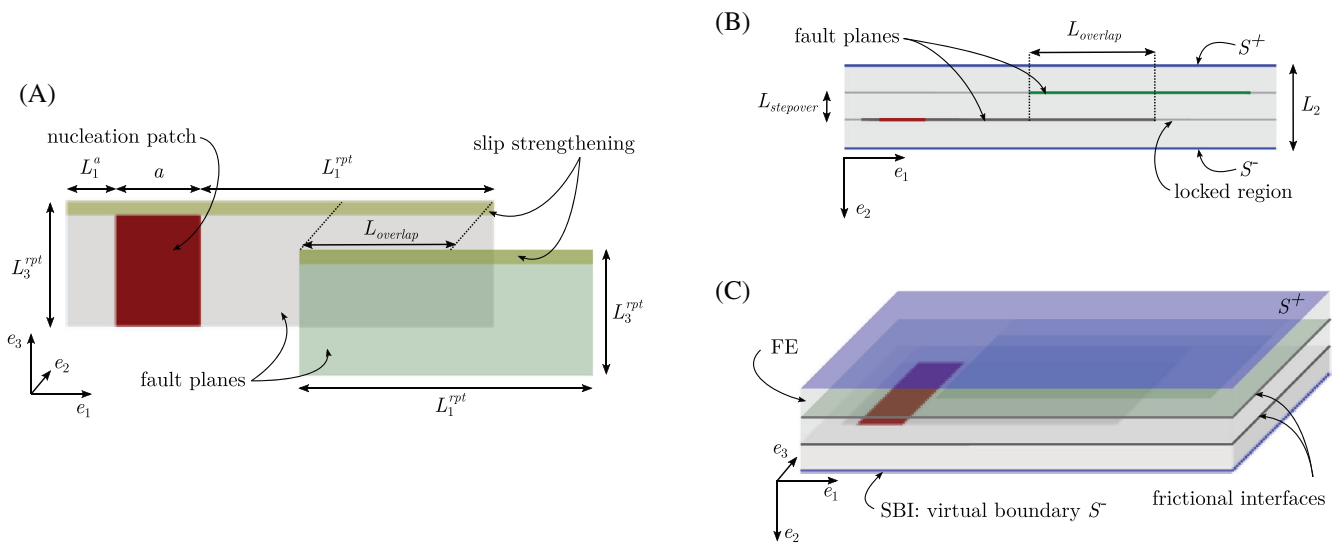

FIGURE 12 Setup of example earthquake rupture in unbounded domain with interacting parallel faults with step-over geometry. (A) Setup geometry. Fault zone regions of rectangular size with $L_1^{rpt} = 40$ km and $L_3^{rpt} = 10$ km, with nucleation over a width $a = 20$ km and the entire seismogenic depth, L_3^{rpt}. To the left of the nucleation patch the extent of the primary fault is $L_1^a = 10$ km. The two fault step-over geometry is characterized by $L_{overlap} = 20$ km and $L_{stepover} = 1$ km, shown in (B). The faults are embedded in a homogeneous elastic medium. (B,C) Hybrid setup: FE domain with SBI as elastodynamic boundary condition. The virtual strip width is $L_2 = 1.4$ km

Note that in this example there are no symmetries. In contrast to the previous examples where the fault plane represented a symmetry axis. As a result of the slip propagation on the primary fault, the normal stress on the secondary fault is not constant. The change in normal stress can reduce or increase the friction strength on the secondary fault, depending on their relative position. Thus, it can hinder or promote the rupture to jump between faults. This class of problems may require regularization of the friction law (Prakash-Clifton correction[58,63,64]) to account for the abrupt normal stress change. However, we are not considering this here.

6.2 | Results

Using the hybrid method, we can successfully reproduce the results of Bai and Ampuero[62] (see Figure 13): after nucleation, the rupture propagates over the primary fault with a nearly vertical front, then the rupture jumps to the secondary fault and, as a consequence of the no-slip boundary condition beyond the depth L_3^{rpt}, the rupture becomes a slip pulse. The wave emitted by the primary rupture successfully nucleates a large rupture on the secondary fault in the forward direction. This example illustrates the ability of the hybrid method to efficiently solve a large and complex simulation and efficiently truncate all incident waves without any artificial reflections. To validate the results of the hybrid method we vary the width of the virtual strip, L_2, and find that also for this example L_2 does not affect the solution.

7 | DISCUSSION

We used a SCEC benchmark problem to validate the hybrid method and then demonstrated its flexibility and superior performance on more complex and heterogeneous problems. The proposed hybrid method takes its flexibility to deal with nonlinearities or bulk heterogeneities from the FEM and its computational efficiency from the SBIM. In particular, since the SBIM provides a perfect wave absorption algorithm there is no artificial wave reflection at the virtual boundary. Thus,
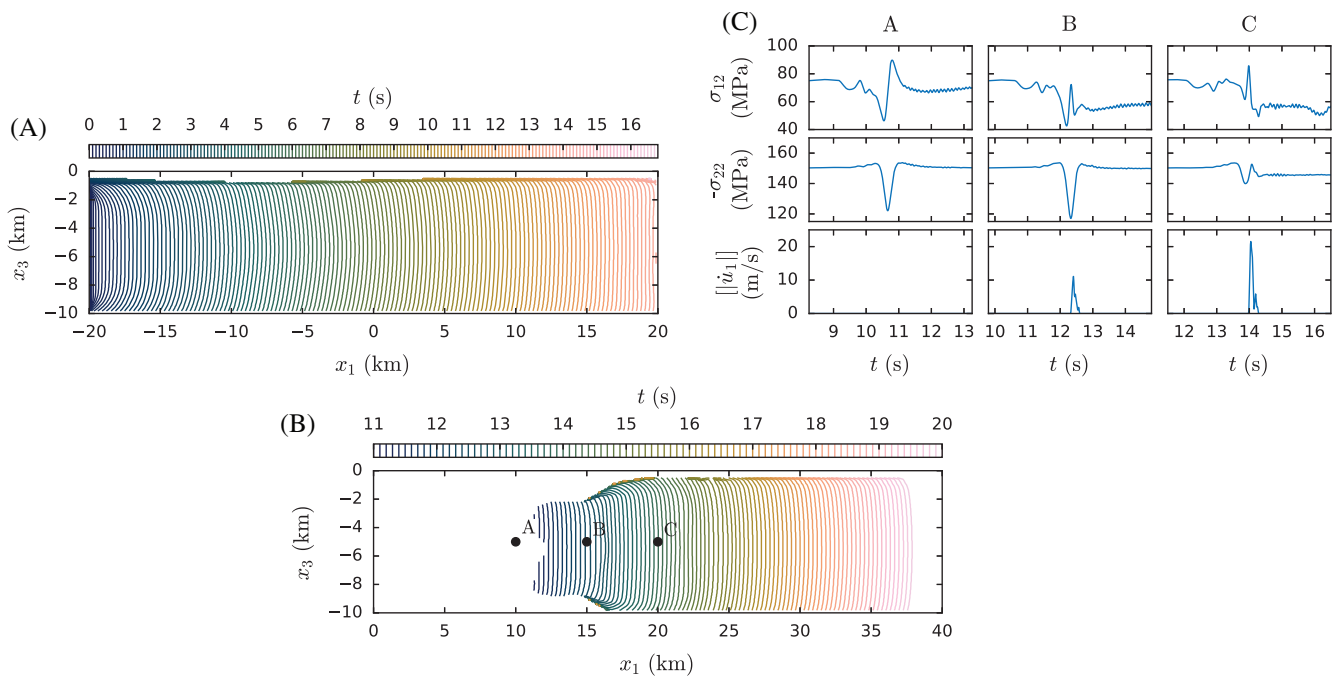

FIGURE 13 Results of example earthquake rupture in unbounded domain with interacting parallel faults with dilational step-over setup and spatial discretization $\Delta x = 100$ m (5M FE-DOF and 0.8M SBI-DOF). (A) Rupture front contour lines on primary fault, where nucleation occurs over region -40 km $< x_1 < -20$ km (not shown). (B) Rupture front contour lines on secondary fault. Rupture transitions from primary to secondary fault. (C) Fault shear, σ_{12}, and normal, σ_{22}, stress and slip rate, $[[\dot{u}_1]]$ at three stations A, B, and C with position on the secondary fault shown in (B)

one can reduce the width of the FEM domain arbitrarily close to the nonlinear or heterogeneous region, as long as the constitutive relation of the bulk beyond the virtual strip can be assumed to be linear.

The computational savings of using the hybrid method—instead of a traditional FEM—can be assessed by considering the complexity of both FEM and SBIM. The complexity of an explicit FEM time step is proportional to the number of degrees of freedom of the FEM problem, that is, $\mathcal{O}(N_1 N_2 N_3)$, where N_i is the number of elements in the i-direction and we assume a regular mesh of hexagonal elements. Similarly, the complexity of an SBIM time step scales with its number of degrees of freedom $\mathcal{O}(N_1 N_3)$. We measured the computation time for a range of simulations with different discretizations and domain sizes, which confirms the linear relationship between computational cost and the number of degrees of freedom (see Figure 14). The computational saving of the hybrid method compared to a standard FEM lies in the reduction of N_2 due to the truncation of the FE domain. Moreover, the added overhead cost of the SBI as wave absorption algorithm is in the same order of magnitude of only one layer of FE elements (see Figure 14B). Therefore, it is practically negligible.

For example, for a full FE simulation, L_2 must be in the order of L_1 to prevent artificial reflections at the domain boundary. However, using the hybrid method the domain size can be truncated up to the extent of the nonlinear region or the extent of the elastic heterogeneity, which are usually one to two orders of magnitude smaller than L_1.[53] Assuming a regular spatial discretization, the domain truncation results in a reduction of N_2 by one order of magnitude and so will the computational cost. The savings may be even higher in other applications.

All our simulations were performed using distributed memory parallel computing with 48 threads and for the largest simulations 96 threads. Therefore, in Figure 14, we report the computational time multiplied by the number of parallel processes. However, the SBIM library that we are using also supports shared memory parallelism and it is designed to be easily coupled to any FEM library written in C++. The only requirement is that the FEM mesh at the virtual boundary $S^\pm$ is a regular grid, due to the spectral representation of the boundary integral equations.

These computational savings represent an important step towards feasible modeling of complex temporal and spatial multi-scale 3D problems such as earthquake cycle simulations with near field heterogeneities, nonlinear material behavior and plasticity, as well as a networks of interacting faults, including fault branches and non-planar fault geometry. The major challenge of earthquake cycle simulations is that they involve very long interseismic loading time (years) while the dynamic rupture happens extremely rapidly (seconds). An advantage of the hybrid method is that the SBIM is already capable of absorbing elastic waves in the dynamic as well as in the quasi-dynamic limit and these approaches can be combined in a variable time stepping scheme, introduced by Lapusta et al.[2] Such a temporal multi-scale simulation couples a quasi-dynamic SBIM with an implicit FEM during the slow loading phase and, once the ruptures become dynamic, it switches to a dynamic SBIM coupled with an explicit FEM—as considered in the current study. These variable time-stepping hybrid method was introduced in a 2D antiplane framework[31] and will be extended to 3D in future work.

Another advantage of the hybrid method is that it could be implemented with any volume based method. For example, if the fault plane is not known a priori, one could use discretization techniques with embedded discontinuities, such as the XFEM[65] or the discontinuous Galerkin.[19]
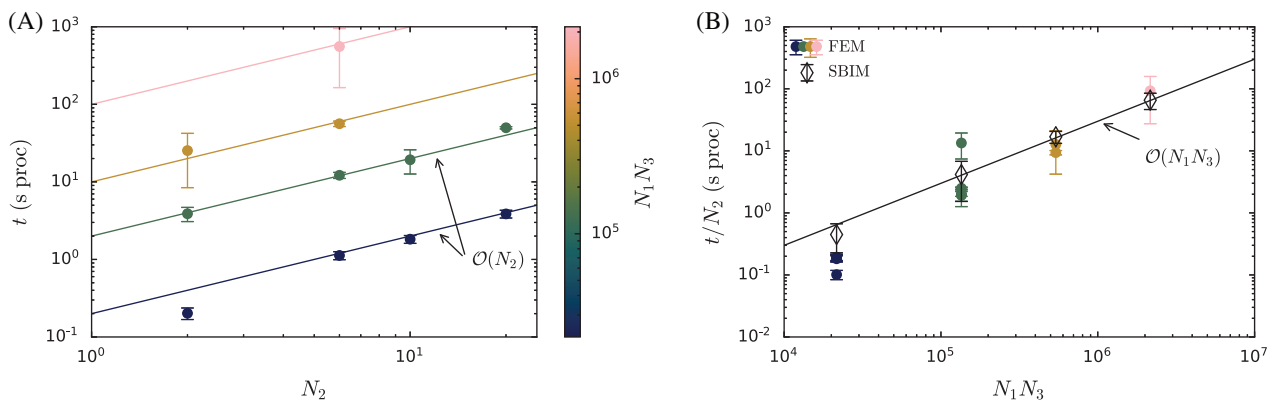

FIGURE 14 Performance study of FEM and Hybrid method. (A) Computation time, t, of a FEM time step as function of width of the virtual strip, that is, number of elements, N_2. Scaling of computational time is shown for a range of frictional interface discretizations, $N_1 N_3$. The complexity of the FEM time step is linear in N_2. (B) Computation time of the FEM time step, t, normalized by N_2 (same data and color-code as in (A)). The computation time of a SBIM time step, when computing the elastodynamic boundary condition for the virtual strip, is equivalent to the computation time for one layer of FEM elements. Both, FEM and SBIM computation times are linear in $N_1 N_3$

8 | CONCLUSION

We developed a three-dimensional hybrid method combining the finite-element method with the spectral boundary-integral method. We validated the hybrid method using a benchmark problem and illustrated its potential for solving complex earthquake propagation on various example problems including systems with near field heterogeneity and multiple interacting faults. The hybrid method is suitable for cases where the spatial extent of near field nonlinearity and heterogeneity is too large to be lumped into an effective fault constitutive law, but is still considerably smaller than the domain of interest for the wave propagation. In these cases, the hybrid method allows for a reduction of computational cost by at least one order of magnitude with respect to a full finite-element implementation, while maintaining the same level of accuracy. The high accuracy and computational efficiency of the hybrid method enable the investigation of complex failure problems such as multi-physics fault zone problems.

DATA AVAILABILITY STATEMENT
The data that support the findings of this study are openly available in ETH Research Collection

ORCID
Gabriele Albertini https://orcid.org/0000-0001-9565-7571
David S. Kammer https://orcid.org/0000-0003-3782-9368

REFERENCES
1. Noda H, Dunham EM, Rice JR. Earthquake ruptures with thermal weakening and the operation of major faults at low overall stress levels. *J Geophys Res Solid Earth*. 2009;114(B7). https://doi.org/10.1029/2008JB006143
2. Lapusta N, Rice JR, Ben-Zion Y, Zheng G. Elastodynamic analysis for slow tectonic loading with spontaneous rupture episodes on faults with rate- and state-dependent friction. *J Geophys Res Solid Earth*. 2000;105(B10):23765-23789. https://doi.org/10.1029/2000JB900250
3. Cochard A, Madariaga R. Dynamic faulting under rate-dependent friction. *Pure and Applied Geophysics PAGEOPH*. 1994;142(3-4):419-445. http://dx.doi.org/10.1007/bf00876049
4. Geubelle PH, Rice JR. A spectral method for three-dimensional elastodynamic fracture problems. *J Mech Phys Solids*. 1995;43(11):1791-1824. https://doi.org/10.1016/0022-5096(95)00043-I
5. Boore DM, Aki K, Todd T. A two-dimensional moving dislocation model for a strike-slip fault. *Bull Seismol Soc Am*. 1971;61(1):177-194.
6. Andrews DJ. Rupture velocity of plane strain shear cracks. *J Geophys Res*. 1976;81(32):5679-5687. https://doi.org/10.1029/JB081i032p05679
7. Das S, Aki K. A numerical study of two-dimensional spontaneous rupture propagation. *Geophys J R Astron Soc*. 1977;50(3):643-668. https://doi.org/10.1111/j.1365-246X.1977.tb01339.x
8. Archuleta RJ, Day SM. Dynamic rupture in a layered medium: the 1966 Parkfield earthquake. *Bull Seismol Soc Am*. 1980;70(3):671-689.
9. Day SM. Three-dimensional simulation of spontaneous rupture: the effect of nonuniform prestress. *Bull Seismol Soc Am*. 1982;72(6A):1881-1902.
10. Virieux J, Madariaga R. Dynamic faulting studied by a finite difference method. *Bull Seismol Soc Am*. 1982;72(2):345-369.
11. Komatitsch D, Tromp J. Introduction to the spectral element method for three-dimensional seismic wave propagation. *Geophys J Int*. 1999;139(3):806-822. https://doi.org/10.1046/j.1365-246x.1999.00967.x
12. Ampuero JP. *Etude physique et numerique de la nucleation des seismes*. PhD thesis. University of Paris VII, France; 2002.
13. Festa G, Vilotte JP. Influence of the rupture initiation on the intersonic transition: crack-like versus pulse-like modes. *Geophys Res Lett*. 2006;33(15). https://doi.org/10.1029/2006GL026378
14. Ma S, Archuleta RJ. Radiated seismic energy based on dynamic rupture models of faulting. *J Geophys Res Solid Earth*. 2006;111(B5). https://doi.org/10.1029/2005JB004055
15. Kaneko Y, Lapusta N, Ampuero JP. Spectral element modeling of spontaneous earthquake rupture on rate and state faults: effect of velocity-strengthening friction at shallow depths. *J Geophys Res Solid Earth*. 2008;113(B9). https://doi.org/10.1029/2007JB005553
16. Käser M, Dumbser M. An arbitrary high-order discontinuous Galerkin method for elastic waves on unstructured meshes – I. the two-dimensional isotropic case with external source terms. *Geophys J Int*. 2006;166(2):855-877. https://doi.org/10.1111/j.1365-246X.2006.03051.x
17. Benjemaa M, Glinsky-Olivier N, Cruz-Atienza VM, Virieux J, Piperno S. Dynamic non-planar crack rupture by a finite volume method. *Geophys J Int*. 2007;171(1):271-285. https://doi.org/10.1111/j.1365-246X.2006.03500.x

18. Puente JDL, Ampuero JP, Käser M. Dynamic rupture modeling on unstructured meshes using a discontinuous Galerkin method. *J Geophys Res Solid Earth*. 2009;114(B10). https://doi.org/10.1029/2008JB006271

19. Pelties C, Puente JDL, Ampuero JP, Brietzke GB, Käser M. Three-dimensional dynamic rupture simulation with a high-order discontinuous Galerkin method on unstructured tetrahedral meshes. *J Geophys Res Solid Earth*. 2012;117(B2). https://doi.org/10.1029/2011JB008857

20. Tago J, Cruz-Atienza VM, Virieux J, Etienne V, Sánchez-Sesma FJ. A 3D hp-adaptive discontinuous Galerkin method for modeling earthquake dynamics. *J Geophys Res Solid Earth*. 2012;117(B9). https://doi.org/10.1029/2012JB009313

21. Cruz-Atienza VM, Virieux J, Aochi H. 3D finite-difference dynamic-rupture modeling along nonplanar faults. *Geophysics*. 2007;72(5):123-137. https://doi.org/10.1190/1.2766756

22. Dalguer LA, Day SM. Staggered-grid split-node method for spontaneous rupture simulation. *J Geophys Res Solid Earth*. 2007;112(B2). https://doi.org/10.1029/2006JB004467

23. Kozdon JE, Dunham EM, Nordström J. Simulation of dynamic earthquake ruptures in complex geometries using high-order finite difference methods. *J Sci Comput*. 2013;55(1):92-124. https://doi.org/10.1007/s10915-012-9624-5

24. Lysmer J, Kuhlemeyer RL. Finite dynamic model for infinite media. *J Eng Mech Div*. 1969;95(4):859-878.

25. Berenger JP. A perfectly matched layer for the absorption of electromagnetic waves. *J Comput Phys* 1994; 1994;114(2): 185–200.

26. Bettess P. Infinite elements. *Int J Numer Methods Eng*. 1977;11(1):53-64. https://doi.org/10.1002/nme.1620110107

27. Erickson BA, Day SM. Bimaterial effects in an earthquake cycle model using rate-and-state friction. *J Geophys Res Solid Earth*. 2016;121(4):2480-2506. https://doi.org/10.1002/2015JB012470

28. Hajarolasvadi S, Elbanna AE. A new hybrid numerical scheme for modelling elastodynamics in unbounded media with near-source heterogeneities. *Geophys J Int*. 2017;211(2):851-864. https://doi.org/10.1093/gji/ggx337

29. Ma X, Hajarolasvadi S, Albertini G, Kammer DS, Elbanna AE. A hybrid finite element-spectral boundary integral approach: applications to dynamic rupture modeling in unbounded domains. *Int J Numer Anal Methods Geomech*. 2019;43(1):317-338. https://doi.org/10.1002/nag.2865

30. Ma X, Elbanna A. Dynamic rupture propagation on fault planes with explicit representation of short branches. *Earth Planet Sci Lett*. 2019;523:115702. https://doi.org/10.1016/j.epsl.2019.07.005

31. Abdelmeguid M, Ma X, Elbanna A. A novel hybrid finite element-spectral boundary integral scheme for modeling earthquake cycles: application to rate and state faults with low-velocity zones. *J Geophys Res Solid Earth*. 2019;124(12):12854-12881. https://doi.org/10.1029/2019JB018036

32. Day SM, Dalguer LA, Lapusta N, Liu Y. Comparison of finite difference and boundary integral solutions to three-dimensional spontaneous rupture. *J Geophys Res Solid Earth*. 2005;110(B12):B12307. https://doi.org/10.1029/2005JB003813

33. Ida Y. Cohesive force across the tip of a longitudinal-shear crack and Griffith's specific surface energy. *J Geophys Res*. 1972;77(20):3796-3805. https://doi.org/10.1029/JB077i020p03796

34. Dieterich JH. Modeling of rock friction: 2. simulation of preseismic slip. *J Geophys Res Solid Earth*. 1979;84(B5):2169-2175. https://doi.org/10.1029/JB084iB05p02169

35. Ruina A. Slip instability and state variable friction laws. *J Geophys Res Solid Earth*. 1983;88(B12):10359-10370. https://doi.org/10.1029/JB088iB12p10359

36. Belytschko T, Liu WK, Moran B, Elkhodary K. *Nonlinear Finite Elements for Continua and Structures*. Wiley; 2013.

37. Courant R, Friedrichs K, Lewy H. Über die partiellen Differenzengleichungen der mathematischen Physik. *Math Ann*. 1928;100(1):32-74. https://doi.org/10.1007/BF01448839

38. Carpenter NJ, Taylor RL, Katona MG. Lagrange constraints for transient finite element surface contact. *Int J Numer Methods Eng*. 1991;32(1):103-128. https://doi.org/10.1002/nme.1620320107

39. Das S. A numerical method for determination of source time functions for general three-dimensional rupture propagation. *Geophys J Int*. 1980;62(3):591-604. https://doi.org/10.1111/j.1365-246X.1980.tb02593.x

40. Andrews DJ. Dynamic plane-strain shear rupture with a slip-weakening friction law calculated by a boundary integral method. *Bull Seismol Soc Am*. 1985;75(1):1-21.

41. Boatwright J, Quin H. The seismic radiation from a 3-D dynamic model of a complex rupture process. Part I: confined ruptures; 1986:97-109; American Geophysical Union (AGU). https://doi.org/10.1029/GM037p0097

42. Das S, Kostrov BV. On the numerical boundary integral equation method for three-dimensional dynamic shear crack problems. *J Appl Mech*. 1987;54(1):99-104. https://doi.org/10.1115/1.3173002

43. Das S, Kostrov BV. An investigation of the complexity of the earthquake source time function using dynamic faulting models. *J Geophys Res Solid Earth*. 1988;93(B7):8035-8050. https://doi.org/10.1029/JB093iB07p08035

44. Israil A, Banerjee P. Two-dimensional transient wave-propagation problems by time-domain BEM. *Int J Solids Struct*. 1990;26(8):851-864. https://doi.org/10.1016/0020-7683(90)90073-5

45. Koller MG, Bonnet M, Madariaga R. Modelling of dynamical crack propagation using time-domain boundary integral equations. *Wave Motion*. 1992;16(4):339-366. https://doi.org/10.1016/0165-2125(92)90022-T

46. Liu Y, Rizzo F. Hypersingular boundary integral equations for radiation and scattering of elastic waves in three dimensions. *Comput Methods Appl Mech Eng*. 1993;107(1-2):131-144. https://doi.org/10.1016/0045-7825(93)90171-S

47. Bonnet M, Bui HD. Regularization of the displacement and traction BIE for 3D elastodynamics using indirect methods. In: Kane JH, Maier G, Tosaka N, Atluri SN, eds. *Advances in Boundary Element Techniques*. Springer Series in Computational Mechanics. Springer; 1993:1-29.

48. Andrews DJ. Dynamic growth of mixed-mode shear cracks. *Bull Seismol Soc Am*. 1994;84(4):1184-1198.

49. Breitenfeld MS, Geubelle PH. Numerical analysis of dynamic debonding under 2D in-plane and 3D loading. *Int J Fract*. 1998;93(1-4):13-38. https://doi.org/10.1023/A:1007535703095

50. de Hoog F, Knight J, Stokes A. An improved method for numerical inversion of laplace transforms. *SIAM J Sci Stat Comput*. 1982;3(3):357-366. https://doi.org/10.1137/0903022

51. Richart N, Molinari JF. Implementation of a parallel finite-element library: test case on a non-local continuum damage model. *Finite Elem Anal Des*. 2015;100:41-46. https://doi.org/10.1016/j.finel.2015.02.003

52. Kammer DS, Albertini G, Ke CY. UGUCA: A spectral-boundary-integral method for modeling fracture and friction. SoftwareX. 2021;15:100785. http://dx.doi.org/10.1016/j.softx.2021.100785

53. Ma X, Elbanna A. Effect of off-fault low-velocity elastic inclusions on supershear rupture dynamics. *Geophys J Int*. 2015;203(1):664-677. https://doi.org/10.1093/gji/ggv302

54. Huang Y, Ampuero JP. Pulse-like ruptures induced by low-velocity fault zones. *J Geophys Res*. 2011;116(B12). https://doi.org/10.1029/2011JB008684

55. Huang Y, Ampuero JP, Helmberger DV. Earthquake ruptures modulated by waves in damaged fault zones. *J Geophys Res Solid Earth*. 2014;119(4):2013JB010724. https://doi.org/10.1002/2013JB010724

56. Huang Y, Ampuero JP, Helmberger DV. The potential for supershear earthquakes in damaged fault zones theory and observations. *Earth Planet Sci Lett*. 2016;433:109-115. https://doi.org/10.1016/j.epsl.2015.10.046

57. Albertini G, Kammer DS. Off-fault heterogeneities promote supershear transition of dynamic mode II cracks. *J Geophys Res Solid Earth*. 2017;122(8). https://doi.org/10.1002/2017JB014301

58. Kammer DS, Yastrebov VA, Anciaux G, Molinari JF. The existence of a critical length scale in regularised friction. *Journal of the Mechanics and Physics of Solids*. 2014;63:40-50. http://dx.doi.org/10.1016/j.jmps.2013.10.007

59. Freund LB. The mechanics of dynamic shear crack propagation. *J Geophys Res Solid Earth*. 1979;84(B5):2199-2209. https://doi.org/10.1029/JB084iB05p02199

60. Kammer DS, Svetlizky I, Cohen G, Fineberg J. The equation of motion for supershear frictional rupture fronts. *Sci Adv*. 2018;4(7):eaat5622. https://doi.org/10.1126/sciadv.aat5622

61. Burridge R. Admissible speeds for plane-strain self-similar shear cracks with friction but lacking cohesion. *Geophys J Int*. 1973;35(4):439-455.

62. Bai K, Ampuero JP. Effect of seismogenic depth and background stress on physical limits of earthquake rupture across fault step overs: fault critical step over jump distance. *J Geophys Res Solid Earth*. 2017;122(12):10280-10298. https://doi.org/10.1002/2017JB014848

63. Prakash V, Clifton RJ. *Time Resolved Dynamic Friction Measurememts in Pressure-Shear*. ASME Applied Mechanics Division-Publications-AMD. Vol 165. ASME; 1993:33.

64. Cochard A, Rice JR. Fault rupture between dissimilar materials: Ill-posedness, regularization, and slip-pulse response. *J Geophys Res Solid Earth*. 2000;105(B11):25891-25907. https://doi.org/10.1029/2000JB900230

65. Liu F, Borja RI. An extended finite element framework for slow-rate frictional faulting with bulk plasticity and variable friction. *Int J Numer Anal Methods Geomech*. 2009;33(13):1535-1560. https://doi.org/10.1002/nag.777